SELECTION OF A SUITABLE WEAR MODEL FOR IMPLEMENTATION IN A GENERIC RAIL DAMAGE FUNCTION

A.A. Meghoe, R. Loendersloot and T. Tinga

University of Twente, Enschede, 7522 NL, Netherlands

a.a.meghoe@utwente.nl
r.loendersloot@utwente.nl
t.tinga@utwente.nl

KEYWORDS: wear, wheel-rail contact, predictive maintenance, remaining useful life

ABSTRACT

Rails often suffer from surface defects caused by wear or Rolling Contact Fatigue (RCF). Therefore, several scientific and engineering models have been developed to predict the evolution of these surface defects. One such model is the Whole Life Rail Model (WLRM), which has been successfully implemented and is also easy to use by rail infrastructure managers for rail maintenance planning. However, this model is developed from a limited number of regions that cannot be considered as a representation of all possible scenarios. Furthermore, the development of such an empirical model is time-consuming. Therefore, developing a theoretical or numerical model, or a combination of both, is required that can be easily adapted for different operational scenarios, including various types of wheel and rail material. The WLRM model consists of three parts: 1) the RCF dominated region, 2) the wear dominated region, and 3) the region with both failure mechanisms interacting with each other. The study in this paper is focused on the wear dominated region as this mechanism is more straightforward compared with RCF. Typically two approaches are used in the literature to model the wear mechanism: 1) based on Archard's wear law and 2) based on the energy dissipation theory. In addition to these models, the authors previously developed a meta-model to reduce computational effort. Furthermore, the embedded wear toolkit in the multi-body software VI-Rail is also used for rail wear calculation. Finally, the most suitable model for implementation in WLRM is shown to be the classical Archard's model because of the local approach, including the spin effect and wide variety of wear coefficients.

INTRODUCTION

Several asset owners, of both the railway infrastructure and the rolling stock, have concluded that the life of their assets is strongly influenced by the wear and RCF mechanisms. Moreover, as the traffic and vehicle speed are increased nowadays, the conditions of the assets, initially designed for specific traffic loads and speed limits, worsen. Therefore, it is important that the amount of damage due to these mechanisms can be predicted as accurately and efficiently as possible. To do so, several damage prediction models that include both failure mechanisms were developed in the past decades. These models include the ratcheting model (Kapoor & Franklin, 2000), the Whole Life Rail Model (WLRM) (Burstow, 2003), and a model in which the shakedown diagram is coupled with a crack propagation law as proposed by Dirks, Enblom, Ekberg, and Berg (2015) and Butini et al. (2019).

Ratcheting model

The ratcheting model was first developed to calculate the amount of wear for ductile materials (Kapoor & Franklin, 2000) and is based on plastic strain accumulation. The material is discretized in *N* rectangular elements, and then for each element, the plastic strain increments ($\Delta\gamma^{ij}$) for a certain number of cycles are summed to reach a certain accumulated plastic strain value (γ^{ij}). Ratcheting failure (wear or crack initiation) occurs when the accumulated plastic strain (γ^{ij}) for one element exceeds a certain critical strain value (γ_c).

The considered element is regarded as weak and removed from the material as wear or remains there and is considered as a crack due to RCF. The plastic strain increment for each element (in column i and row j) per cycle is calculated as follows (Franklin, Chung, & Kapoor, 2003):

$$\Delta\gamma^{ij} = C\left(\frac{{\tau_{zx(max)}}^{j}}{k_{\text{eff}}^{ij}} - 1\right) \qquad \textit{Equation 1}$$

And the accumulated plastic strain is then updated as follows:

$$\gamma^{ij} = \gamma^{ij} + \Delta\gamma^{ij} \qquad \textit{Equation 2}$$

where $\tau_{zx(\max)}^{j}$ is the maximum orthogonal shear stress at the depth of row j, C is a material constant and k_{eff}^{ij} is the effective shear yield stress that is calculated as follows:

$$k_{\text{eff}}^{ij} = \beta k_0 \max\left\{1, \sqrt{1 - e^{-\alpha\gamma^{ij}}}\right\} \qquad \textit{Equation 3}$$

and α and β are material constants and k_0 is the initial yield stress.

The input parameters required for the plastic strain calculation are obtained from two processes. The first process is a multi-body dynamic simulation to determine the contact conditions like contact pressure and contact geometry. The second process is calculating the maximum orthogonal shear stress derived from the subsurface stresses in the material. The subsurface stresses can be calculated using Finite Element Methods or in the semi-analytical half space (Santos, Santos Jr., & Bruni, 2004). Therefore, the ratcheting model is considered a time-consuming approach if various scenarios must be evaluated.

Whole Life Rail Model

The WLRM was developed by Burstow (2003) from field observations and numerical modelling to determine the probability of RCF on rails for steel grade R220. Hiensch and Steenbergen (2018) performed similar field tests and concluded that the WLRM curve for steel grade R260 (UIC 900A) is similar to the R220 curve, which shows that the model has the generality to capture the main failure mechanism phenomena.

The WLRM is based on the dissipated energy in the wheel-rail contact, and the resulting damage index D, i.e. the amount of damage caused per cycle or wheel passage, depends on the wear number $T\gamma$ which can be calculated as:

$$T\gamma = T_x\gamma_x + T_y\gamma_y \qquad \textit{Equation 4}$$

where T_x and T_y represent the tangential or shear forces and γ_x, γ_y the longitudinal and lateral creepages, respectively.

The wear number ($T\gamma$) can be obtained from multi-body dynamic simulations and determines which degradation mechanism (RCF or wear) is dominant on a specific piece of track that is subjected to certain loading conditions. For example, the loading conditions on line section A-B in Figure 4 represent the RCF dominant region, C-D the wear dominant region, while B-C corresponds with to a combination of RCF and wear. Failure (i.e. crack initiation) occurs when the summation of the damage index D_{i} (i.e. damage contribution per cycle) reaches unity after N load cycles (Palmgren-Miner rule):

$$D = \sum_{i=1}^{N} D_i \qquad \textit{Equation 5}$$

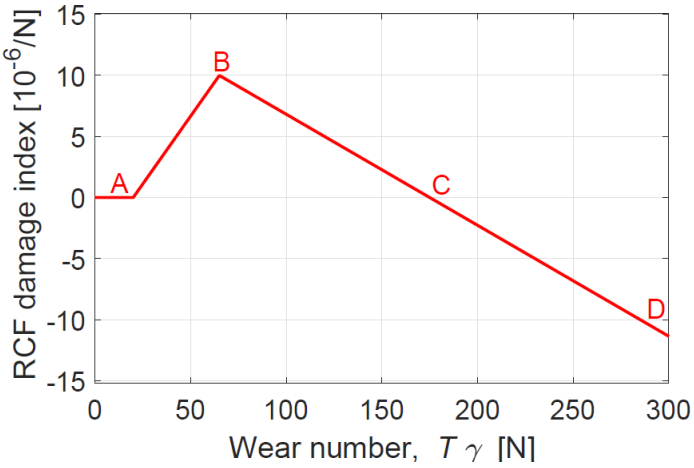

Figure 1: RCF damage index as a function of the wear number (Dollevoet, 2010).

The advantages of the WLRM are: 1) the input parameter required for the damage evaluation for the WLRM is a single variable (e.g. wear number), and 2) the interaction between wear and RCF is incorporated. The disadvantage of the WLRM is the time required to do the field observations for specific wheel and rail material at specific track locations and for specific trains (Meghoe, Loendersloot, & Tinga, 2019) to determine the total number of cycles to failure or crack initiation (that yield the damage index values in the diagram). Therefore, the goal is to find a more generic rail life model that is independent of the region or scenario and uses primarily analytical analyses and numerical simulations.

Shakedown diagram

In the shakedown diagram, see Figure 2, the normalized vertical load is plotted against the utilized friction coefficient. From the shakedown diagram, which is based on the Hertzian contact theory, the effect of shear stress on the rail fatigue behavior can be determined (Ekberg, Akesson, & Kabo, 2014). This effect is quantified by the surface fatigue index (FI_{surf}), which acts as a measure for the risk of crack initiation.

$$FI_{\text{surf}} \equiv \mu - \frac{2\pi abk}{3\,F_z} \qquad \textit{Equation 6}$$

A value $FI_{\text{surf}} > 0$ corresponds to a scenario with plastic deformation that leads to crack initiation. The input for FI_{surf} consists of three main parameter groups: the acting loads, contact geometry and material strength. F_z is the normal contact force, k is the yield stress in shear, a and b are the semi-axis of the contact ellipse, and μ is the utilized friction coefficient which is determined from the acting tangential (F_x, F_y) and normal (F_z) forces:

$$\mu = \frac{\sqrt{{F_x}^2 + {F_y}^2}}{F_z} \qquad \textit{Equation 7}$$

The input parameters of FI_{surf} related to acting loads and contact geometry are obtained from numerical simulations of vehicle-track interaction, which are typically conducted with multi-body dynamic codes. The

shakedown diagram (Figure 2) shows which material response can be expected for certain normal load and friction coefficient combinations. The surface fatigue index FI_{surf} then quantifies the distance between the Working Point (WP, the actual situation) and the threshold value (curve BC) for ratcheting. A negative value represents a safe situation. The disadvantages of the shakedown approach are that it is focussing on RCF only and that the crack size cannot be determined from this graph. However, Dirks et al. (2015) and Butini et al. (2019) have shown that by including a Basquin-like relation, the crack propagation is covered and the predicted crack length (c_p) can be calculated by using the following equation:

$$c_p = \frac{1}{\alpha(a\ \sigma)^{\beta}} \qquad \textit{Equation 8}$$

Where α and β are material parameters that should be calibrated and a = 1MPa^{-1} (Butini et al., 2019). Furthermore, the deficiency in analyzing the interaction between wear and RCF is ruled out, as the crack depth can be adjusted based on the calculated wear depth. Note that the wear depth will be calculated by an already established wear law. Although the results obtained from previous studies are encouraging, the drawback of this approach is that the characterization of the specific damage law requires specific experimental fatigue tests.

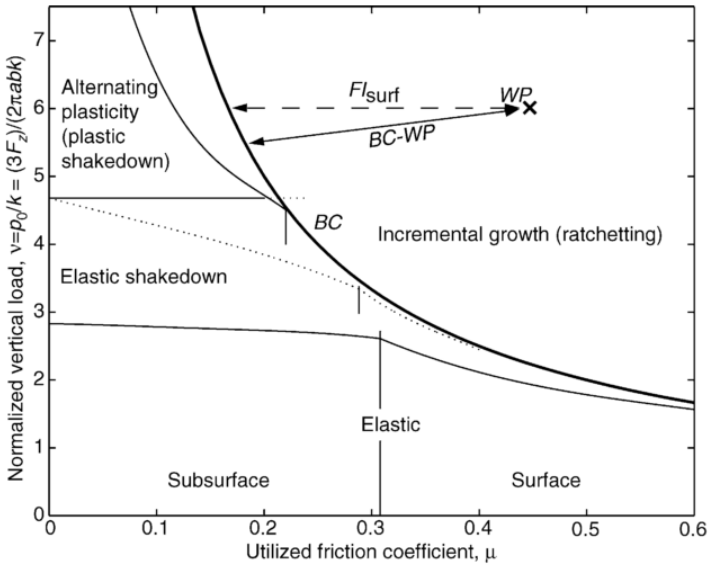

Figure 2: Shakedown diagram (Ekberg et al., 2014).

After reviewing all RCF and wear combination models, it can be concluded that the ratcheting model's numerical complexity is unsuitable for a computationally efficient prognostic framework. The combination of the shakedown diagram and the Basquin-like relation is also not feasible due to the experimental tests that need to be carried out. Zacher (2009) implemented the Whole Life Rail Model for two curves with mixed traffic and found a good correlation between predicted cracks and detected cracks from field observations. However, the disadvantages of this approach are the computation time required to evaluate the additional traffic and track geometry scenarios in combination with detailed vehicle models and the material dependency.

The aim is to achieve a generic model to evaluate wear and RCF on the track simultaneously. From the models described above, the WLRM would be a good choice, given the ease and simplicity of working with it. However, to obtain a generic model, the relevant parameters to construct the WLRM should be understood. In this study, the wear dominated region in Figure 1 will be reconstructed using existing wear laws, namely Archard's wear law and the energy dissipation approach. Besides that, the wear evaluation will also be carried out using meta-models that the authors derived from Archard's law for a relevant set of different scenarios

(Meghoe et al., 2019) to reduce computational effort. The structure of the remainder of this paper is as follows: first, wear models are described, followed by a description of the utilized methodology, the results and discussion, and finally, the conclusions and future work are presented.

WEAR MODELS

This section will briefly describe the most commonly used rail wear models, the specific rail-wheel material combination they were developed from, and the classification of the global vs. local approach. Most wear laws can be applied globally or locally. In the global approach, the amount of worn material is calculated from the global forces and creeps. While the local approach takes into account the distribution of tangential stresses and slip velocity per discretized element in the contact patch. Typically, there are two types of wear laws: the first is based on normal contact load and sliding speed (i.e. Archard's law) and the second is based on the energy dissipation theory. For a more detailed review of the existing numerical wheel and rail wear models the reader is referred to the work of Bosso, Magelli, and Zampieri (2022).

Archard's wear law

Archard developed a sliding wear model for metal to metal contact surfaces based on theoretical and experimental studies (Archard, 1953). Therefore, Archard's wear law can also be applied to wheel-rail contacts and indicates that the amount of wear volume loss [mm^3] is related to sliding distance s [mm], normal force F_N [N] and hardness H of the softer material [N/mm^2] (Archard, 1953):

$$V = k \frac{s F_N}{H} \qquad \textit{Equation 9}$$

This wear law can also be applied locally when the contact area is discretized in a number of elements, and the amount of material lost is evaluated per element.

$$h(x,y) = k \frac{s(x,y)p(x,y)}{H} \qquad \textit{Equation 10}$$

where x and y are the longitudinal and lateral coordinates of the discretized element, p is the normal pressure [N/mm^2], and h is the vertical wear depth [mm].

The wear coefficient k depends on the surface conditions and is usually determined empirically, e.g. by pin on disk or twin disc configuration measurements. For simple calculations, the wear coefficient for rail and wheel steels can be derived from the wear map of Jendel (2002), see Figure 3. This map was formed from a series of pin-on-disc and twin-disc experiments for various contact pressure, sliding velocity and hardness during dry contact conditions and for rail material 900A and R7 wheel (Jendel, 2002). R. Lewis and Olofsson (2004) carried out experiments to determine the wear coefficients for several rail and wheel materials. One can use a specific wear coefficient obtained from their study if the wheel-rail material combination is the same, or, as is common practice, calibrate the wear coefficient based on field data. However, this latter option is no longer valid if new materials are introduced. According to Li, Jin, Wen, Cui, and Zhang (2011), the wear coefficient for the wheel-rail contact is mainly in the region between [1-10] and [30-40] of the wear map, whereas [300-400] is considered to be the region for severe wear (Brouzoulis, 2014).

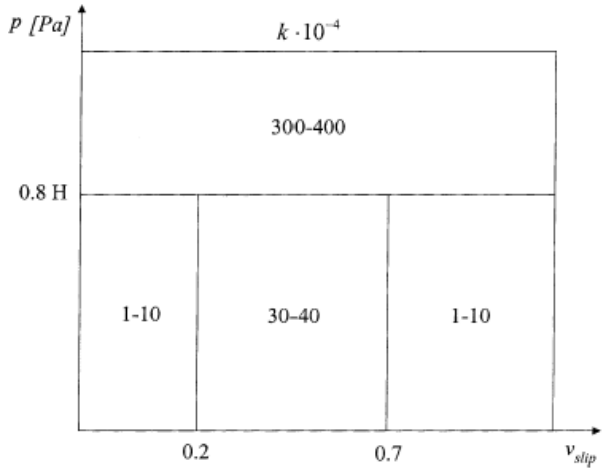

Figure 3: Wear chart for the wear coefficient based on laboratory measurements with wheel and rail steels (Jendel, 2002).

Meta-models based on Archard's law

The meta-model developed by Meghoe et al. (2019) considered the UIC 900A rail material and s1002 wheel material. As mentioned before, these models are based on Archard's law and are in the form of second-order polynomials, which are defined as follows:

$$y(\boldsymbol{x}) = \beta_0 + \sum_{i=1}^{n} \beta_i x_i + \sum_{i=1}^{n} \beta_{k+i} {x_i}^2 + \sum_{i=1}^{n-1} \sum_{j>i}^{n} \beta_{i,j} x_i x_j \qquad \textit{Equation 11}$$

where y is the rail wear area in mm^2, $\boldsymbol{x}$ is the vector of x_i which are the various input parameters and β_i are the fitted model parameters. A flowchart of the meta-model approach is presented in Figure 4.

The rail wear prediction model has nine input parameters (n=9): axle load, curve radius, vehicle speed, the longitudinal and lateral stiffness of the primary bogie, rail profile geometry, material hardness, friction coefficient and rail cant. Furthermore, the rail profile geometry is represented by the measured vertical wear depth at the rail head.

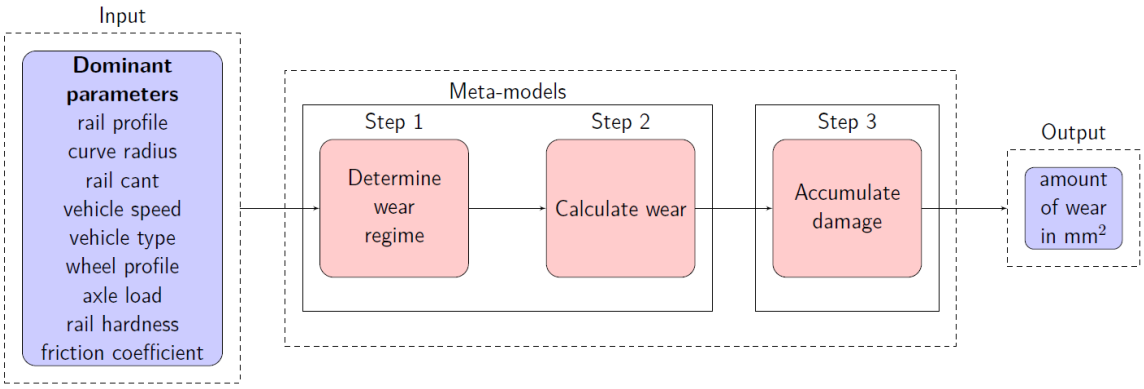

Figure 4: *Rail wear estimation process by means of meta-models (Meghoe et al., 2019).*

Energy-based approach from Zobory (as used in VI-Rail)

Besides Archard's law, which describes the proportionality between the amount of material lost and the normal load and sliding distance, other models based on the energy dissipation or frictional work in the wheel-rail contact area are frequently used for rail or wheel wear prediction. Zobory (1997) developed three models applicable to wheel-rail contact problems: Dissipated Energy Based Wear Hypothesis, Normal Traction Based Wear Hypothesis and Simplified-Combined Wear Hypothesis. In the first model, the proportionality between the energy and mass flow density at an arbitrary point r_p occurring at time t, is achieved by calculating the energy dissipation for the adhesive and sliding part of the contact patch separately:

$$\dot{m}_d(r_p, t) = k^* \dot{E}_d(r_p, t) \qquad \textit{Equation 12}$$

Where $\dot{m}_d$ and $\dot{E}_d$ are the mass and energy flow density, and k^* is the wear coefficient determined by Zobory (1997) from several experimental studies, see Figure 5.

The disadvantage of the first model that Zobory (1997) proposed is that it is time-consuming; therefore, the Normal Traction Based Wear Hypothesis was developed. This hypothesis neglected the separation of the contact area and was based on the correlation between mass flow density, normal traction and slip velocity. Therefore, this model belongs to the global approach category. The third model was developed for a smooth implementation in the vehicle dynamics model, such as in the VI-Rail commercial software, and is a combination of the previous two models. The wear module, including the wear coefficient in VI-Rail, was calibrated using the results with measured data for a curved section of S-Bahn Stuttgart, Germany (VI-Grade, 2016).

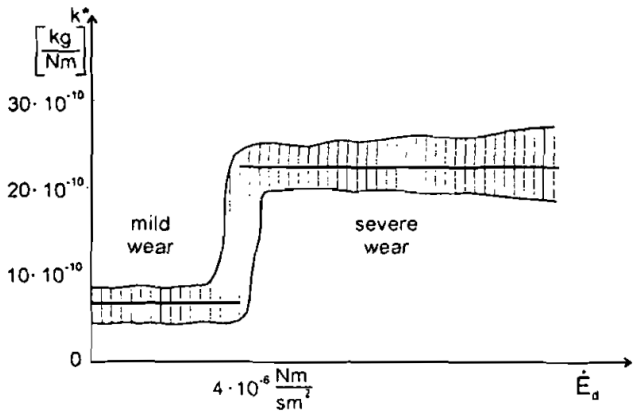

Figure 5: Domains of mild and severe wear (Zobory, 1997).

Energy-based approach from Bolton and Clayton

Bolton and Clayton (1984) obtained experimental wear rate results from twin-disc testing using several wheel and rail material combinations under which UICA rail material and class D tyre steel for the wheel, see Figure 6. They confirmed that there are three wear regime types and suggested the following relation for wear regime type II:

$$\frac{W}{Ad} = K_1 \frac{T\gamma}{A} + K_2 \qquad \textit{Equation 13}$$

Where W is the amount of material lost in [mg], A is the contact area in [mm^2], d is the rolled distance in [m], and K_1 and K_2 are constants comparable to wear coefficients. This model is, however, only applicable when using the global approach.

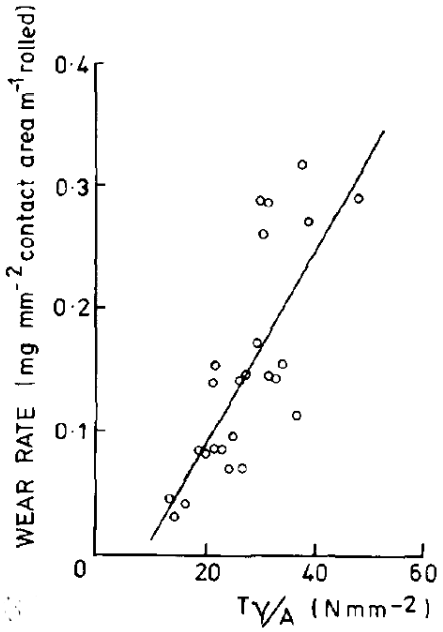

Figure 6: Type II wear rate plotted against $T\gamma/A$ for UICA rail steel (Bolton & Clayton, 1984).

Energy-based approach from Lewis et. al

Lewis (Braghin, Lewis, Dwyer-Joyce, & Bruni, 2006; R. Lewis et al., 2003; R. Lewis & Olofsson, 2004) conducted twin-disc experiments where the rail disc (UIC 900A material) was used as the braking disc and the wheel disc (R8T steel) as the driving disc. The outcome of these experiments was similar to Zobory's model, namely the wear rate is proportional to the dissipated energy $T\gamma$ (product of tangential stress and slip):

$$Wear\ Rate = K\ \frac{T\gamma}{A} \qquad \textit{Equation 14}$$

where A denotes the contact patch area. The difference between this energy dissipation model and Zobory's model is that it defines a clear distinction between the three wear regimes with different wear coefficients K for each region (R. Lewis & Olofsson, 2004). From Figure 7 it can be seen that the distinction in regimes is caused by different contact conditions (see x-axis). Furthermore, this model cannot only be applied globally, but also locally, as $T\gamma/A$ can be evaluated for each discretized element.

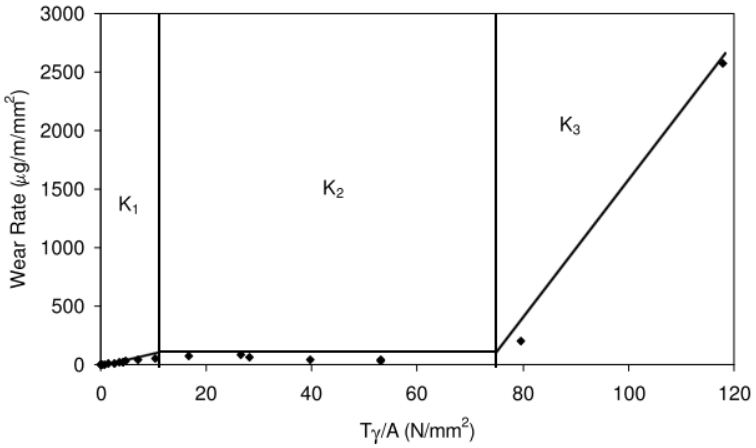

Figure 7: Wear regimes and coefficients (R. Lewis & Olofsson, 2004).

To be able to compare the wear rates obtained from Archard's approach and the energy approach, a similar variable should be used. Hence, the wear rate from the energy approach is divided by the steel density value (7850 kg/m3), which then yields the wear rate in wear area per contact area (i.e. dimensionless). Furthermore, for Archard's law, the worn area for each elliptic contact area is calculated and then divided by the magnitude of the elliptic contact area. In this way, both approaches use the same definition for the wear rate.

RESULTS AND DISCUSSION

In this section, the different wear models, i.e. the wear model based on Archard's law, meta-model and energy dissipation theory, are compared with each other, with the wear results obtained from the VI-Rail wear toolkit and with the wear rate obtained by Bolton and Clayton (1984) and R. Lewis and Dwyer-Joyce (2006). First, a single case or scenario is considered to compare the wear depth distribution along the lateral axis of the contact patch. Second, multiple cases or scenarios are considered to compare the wear area for different contact conditions. After that, preliminary results for the reconstruction of the wear dominated region of the WLRM will be presented.

Rail wear evolution

The rail wear prediction procedure consists of three parts:

1. Perform multi-body dynamics simulations to calculate contact forces, contact points and contact areas.
2. Implement a local wheel-rail contact model using Hertz contact theory and the FASTSIM algorithm to determine the contact conditions, such as the normal and tangential stress distributions.
3. Apply a local or global wear model, e.g. Archard's wear law or energy dissipation approach.

In this study, 200 scenarios using wheel profile s1002 and rail profile UIC54 (steel grade R260) are created using the Design of Experiments methodology, which are then simulated in the multi-body dynamics software VI-Rail. The output of the vehicle dynamics simulations is used as input for the local contact and wear models. Therefore, the wear number ($T\gamma$) is also obtained from multi-body dynamic simulations. In addition, Bosso et al. (2022) have presented a more detailed review of the existing numerical wheel and rail wear models.

Wear models comparison: single scenario

The input parameters that were considered for the single scenario case with wheel s1002 and rail UIC60 are presented in the Appendix, see Table 3. Table 1 shows the wear rate results for the different models along with the computation time. As expected, the meta-model has the lowest computation time, however, the time required to develop the meta-model is not considered. The computation time of the VI-Rail wear toolkit is lower than Archard's law and the energy dissipation theory because the evaluation of wear is already implemented in the toolkit. For the other two methods, a dynamic simulation is first performed in VI-Rail, after which the contact parameters are extracted and exported to the MATLAB environment for the wear evaluation process. The wear evaluation for the first three models in Table 1 follows a local approach, i.e. wear is evaluated per discretized element of the contact area. The vertical wear depth distribution along the lateral direction of the contact ellipse is depicted in Figure 8. It can be seen that the vertical wear depth distribution is somewhat different due to the definition of slip and wear coefficients. However, Table 1 shows that the total amount of wear in the first three models is similar. The results obtained from the meta-model are different because the meta-model was fitted for a wheel (s1002) in worn condition and another rail profile (UIC54). This does not affect the computational efficiency compared to the other models.

Table 1: Wear results for different wear models (single scenario).

Wear model	**Max vertical wear depth [m]**	**Total wear area [mm^2]**	**Computation time [seconds]**
VI Rail wear toolkit	1.0491e-04	8.4071e-04	125.0
Archard's law	1.2837e-04	8.8386e-04	142.5
Energy dissipation theory	1.1292e-04	8.4236e-04	140.0
Meta-model	-	1.4004e-04	1.5

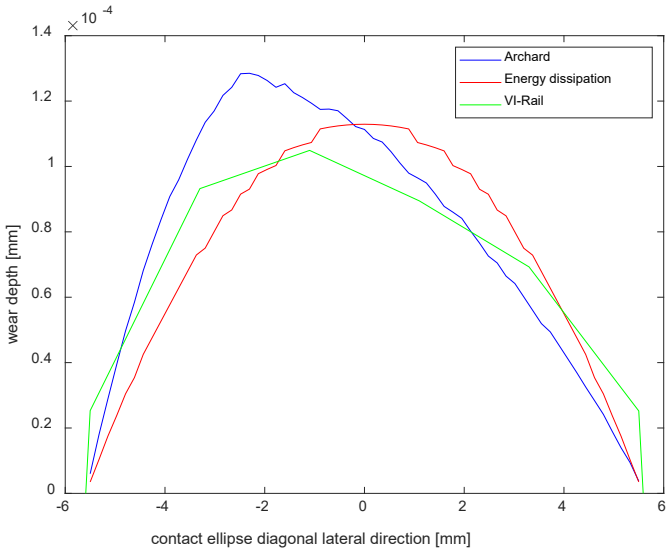

Figure 8: Vertical wear depth distribution along the lateral direction of contact ellipse.

Wear models comparison: multiple scenarios

Figure 10 depicts the wear rate results based on Archard's law, energy dissipation theory, meta-models, and the wear rate of Bolton and Clayton (Bolton & Clayton, 1984) and R. Lewis and Dwyer-Joyce (2006). Each data point is a representation of the wear rate for one single simulation (or scenario) using wheel s1002 (in

worn condition) and UIC54. It can be seen that the wear results are evenly distributed around the wear rate of Lewis et al., with some outliers that are clearly presented in Figure 10. This figure also shows that most of the data points obtained with Archard's law are located at the same level as the measured results in Figure 7. The input parameters for the multiple scenarios can be found in the Appendix. Furthermore, the difference between the wear rate of Bolton and Clayton and Lewis et al. results from the different wheel materials. Bolton and Clayton used Class D Tyres for the wheel, and Lewis and Dwyer-Joyce used the R8T wheel. Lewis et al. (2010) also concluded this, after performing experiments to obtain the wear rate for Class D Tyre vs BS11 rail material, R8T vs 900A and R7T vs 900A.

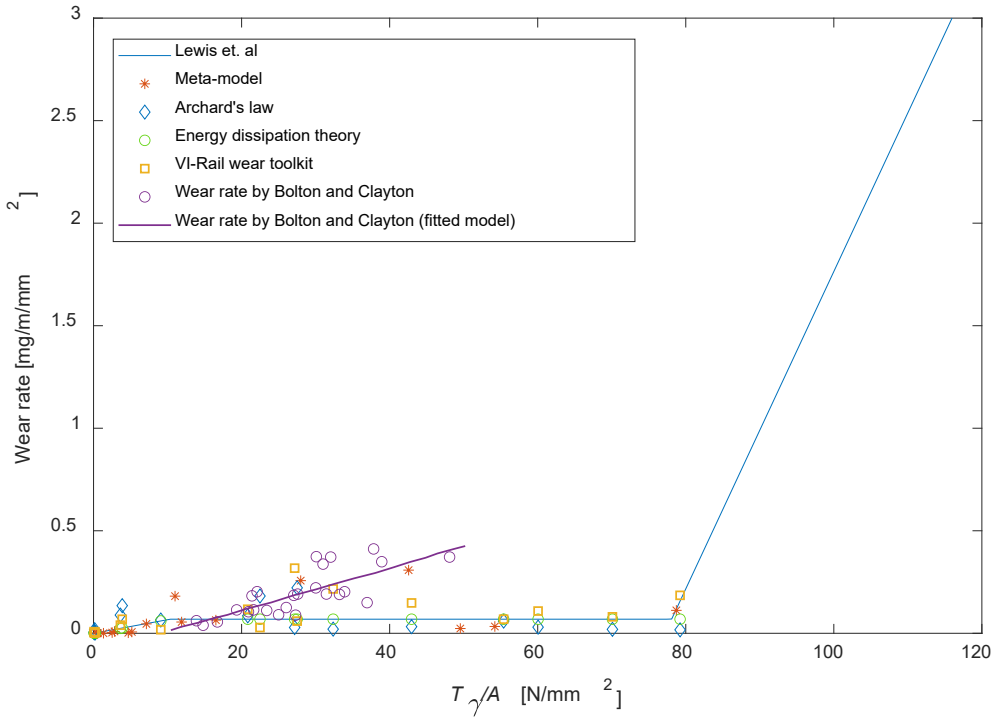

Figure 9: Wear rate results for multiple scenarios by using different models.

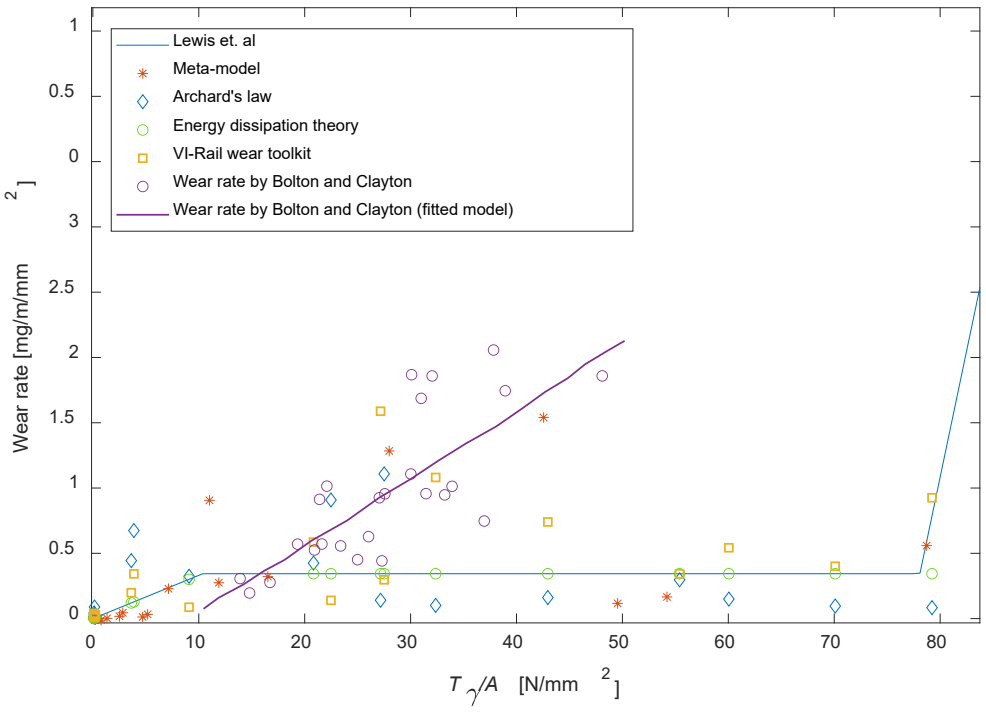

Figure 10: Wear rate results for multiple scenarios by using different models (zoomed in).

Wear-dominated region WLRM

To reconstruct the wear function of the WLRM from numerical results (instead of field observations), the wear rate must be converted into a number of cycles to failure denoted by N, as this quantity is on the vertical axis in the WLRM, see Figure 1. It is therefore proposed here to calculate the number of cycles (i.e. passing train wheels) that it takes for the wear process to remove a typical fatigue crack. If the wear rate succeeds to remove the cracks entirely, the wear mechanism is the dominant mechanism and failure due to RCF is not a concern. Dirks et al. (2015) showed that cracks propagate at an angle between 15° and 30° into the rail. Therefore, in this study, it is assumed that a typical RCF crack propagates under an angle of 20° into the rail and has an average length (L) of 2 mm. It then requires a wear depth (h) of 0.68 mm to remove this crack entirely. With this information, the number of cycles required to accumulate the required wear area can be calculated.

Choosing the most suitable approach for rail wear prediction is quite challenging without any test or field data. From Table 1, the total amount of wear calculated with the meta-model differs from the other three approaches. This is because the meta-model was fitted for the combination of wheel s1002 and rail UIC54. Therefore, a generalisation of the WLRM with this model will be inefficient as each time a new meta-model needs to be fitted. The energy approach is also not chosen here because the contact forces and creepages obtained from VI-Rail version 17.0 do not include the spin creepage (Enblom & Berg, 2005). Including the spin effect in future work and using the local approach is recommended. In this work, the global approach version of this model was applied. The approach used in the VI-Rail wear toolkit can also be regarded as a global approach, as the wear depth is not calculated per discretized element, and the spin creepage is not included (VI-Grade, 2016). Hence, the wear rate based on Archard's law is chosen here for the reconstruction of the wear part of the WLRM, as this is a local approach and also considers the spin creepage. Furthermore, the wear coefficients from Jendel's wear map (Figure 3), used in Archard's law, allow for a wider variety of wear coefficients obtained from different wheel and rail materials combinations.

Figure 11 depicts the obtained damage index, in number of cycles to failure per unit force based on Archard's wear law and the wear rate of the WLRM as derived for R220 from the work of Burstow (Burstow, 2004)or a friction coefficient of 0.4. In total 200 scenarios, with different input parameters, using wheel profile s1002 and rail profile UIC54 (steel grade R260) are taken into account using the LHS methodology. Figure 11 shows that the position, but not the slope, of the actual trend line of the wear functions with friction coefficients 0.4, 0.5 and 0.6 deviates from the WLRM wear function. This is because wear only occurs after exceeding a certain threshold value for the wear number ($T\gamma$), as for lower values of shear force and creepage, the wear mechanism is not activated (Bolton & Clayton, 1984). Bolton and Clayton explained that the wear mode requires some activation energy to start the wear process. Figure 11 shows that the clusters do have the same starting point on the x-axis ($T\gamma$). However, further research is required to study the small number of data points before this threshold. Furthermore, there are two groups of data points: the lower data points correspond with wear regime 1 (green dashed ellipse), and the upper ones with wear regime 2 (red dashed ellipse), see Figure 3. This suggests that the damage index is dominated by wear regime 2, since the trends of the wear functions show a similar slope as the WLRM function.

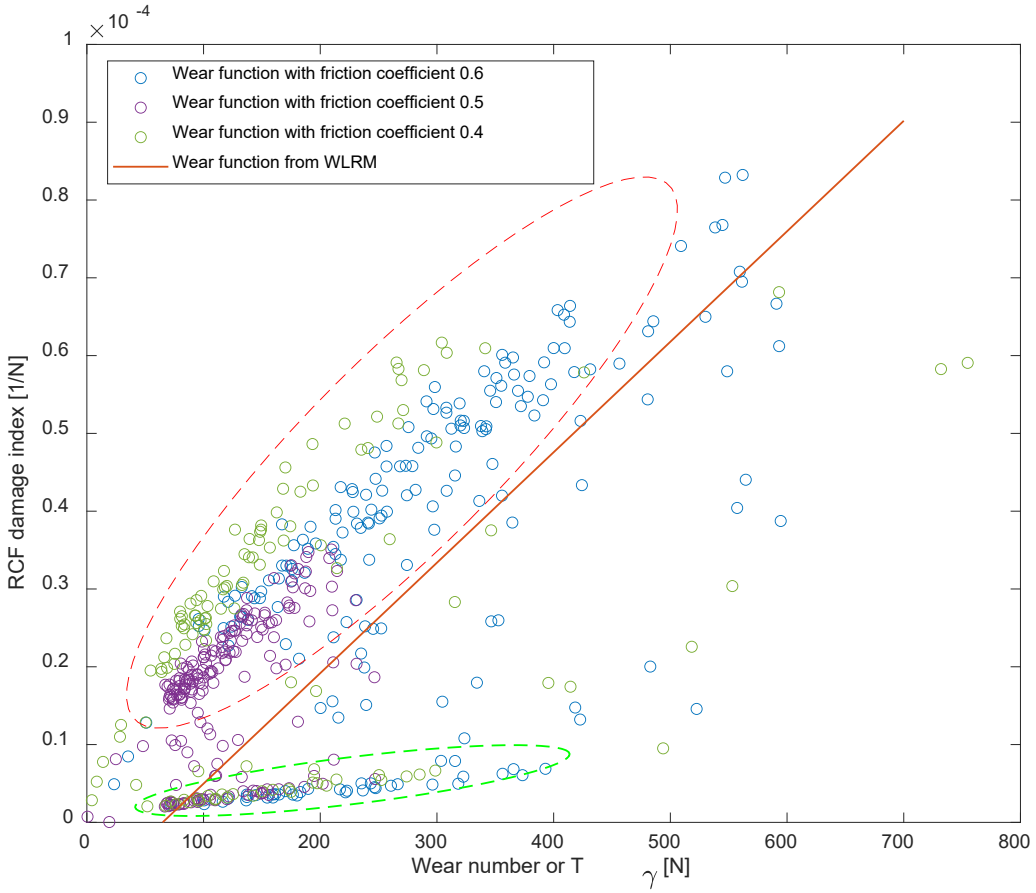

Figure 11: WLRM wear function compared to wear rate results based on Archard's law.

CONCLUSION AND FUTURE WORK

The ultimate goal is to find a more generic rail life model by removing the dependency on specific regions or scenarios and using primarily analytical analyses and numerical simulations. As a first step, the objective of this study was to select a suitable approach for the rail wear calculation part in the Whole Life Rail Model. The wear results from Archard's law, meta-model, energy dissipation theory and the VI-Rail wear toolkit were

compared with each other. The different wear models showed similar results except for the meta-model due to different wheel-rail combination. But as the classical Archard's law follows the local approach, considers the spin creepage and allows for a wider variety of wear coefficients, this model was chosen for the reconstruction of the WLRM wear function. Thereafter, the wear function from the WLRM was compared to the wear function for different friction coefficient values, and an offset was noticed, which can be explained in terms of the wear threshold. The slopes of the trends are similar to the WLRM wear function. In conclusion, the results are promising, and in the future, the authors hope to validate the research with experimental work and field observations.

REFERENCES

Archard, J. F. (1953). Contact and Rubbing of Flat Surfaces. *Journal of Applied Physics, 24*(8), 981-988. doi:10.1063/1.1721448

Bolton, P. J., & Clayton, P. (1984). Rolling Sliding Wear Damage in Rail and Tyre Steels. *Wear, 93*(2), 145-165. doi:10.1016/0043-1648(84)90066-8

Bosso, N., Magelli, M., & Zampieri, N. (2022). Simulation of wheel and rail profile wear: a review of numerical models. *Railway Engineering Science, 30*(4), 403-436. doi:10.1007/s40534-022-00279-w

Braghin, F., Lewis, R., Dwyer-Joyce, R. S., & Bruni, S. (2006). A mathematical model to predict railway wheel profile evolution due to wear. *Wear, 261*(11-12), 1253-1264. doi:10.1016/j.wear.2006.03.025

Brouzoulis, J. (2014). Wear impact on rolling contact fatigue crack growth in rails. *Wear, 314*(1-2), 13-19. doi:10.1016/j.wear.2013.12.009

Burstow, M. C. (2003). *Whole Life Rail Model application and development: Development of a rolling contact fatigue damage parameter*. Retrieved from UK: Rail Safety and Standards Board

Burstow, M. C. (2004). *Whole life rail model application and development for RSSB (T115) - continued development of an RCF damage parameter*. Retrieved from

Butini, E., Marini, L., Meacci, M., Meli, E., Rindi, A., Zhao, X. J., & Wang, W. J. (2019). An innovative model for the prediction of wheel - Rail wear and rolling contact fatigue. *Wear, 436*, 203025. doi:10.1016/j.wear.2019.203025

Dirks, B., Enblom, R., Ekberg, A., & Berg, M. (2015). The development of a crack propagation model for railway wheels and rails. *Fatigue & Fracture of Engineering Materials & Structures, 38*(12), 1478-1491. doi:10.1111/ffe.12318

Dollevoet, R. P. B. J. (2010). *Design of an Anti Head Check Profile Based on Stress Relief.* (PhD), University of Twente, Enschede, The Netherlands.

Ekberg, A., Akesson, B., & Kabo, E. (2014). Wheel/rail rolling contact fatigue - Probe, predict, prevent. *Wear, 314*(1-2), 2-12. doi:10.1016/j.wear.2013.12.004

Enblom, R., & Berg, M. (2005). Simulation of railway wheel profile development due to wear - influence of disc braking and contact environment. *Wear, 258*(7-8), 1055-1063. Retrieved from <Go to ISI>://WOS:000227273800013. doi:10.1016/j.wear.2004.03.055

Franklin, F. J., Chung, T., & Kapoor, A. (2003). Ratcheting and fatigue-led wear in rail-wheel contact. *Fatigue & Fracture of Engineering Materials & Structures, 26*(10), 949-955. doi:DOI 10.1046/j.1460-2695.2003.00703.x

Hiensch, M., & Steenbergen, M. (2018). Rolling Contact Fatigue on premium rail grades: Damage function development from field data. *Wear, 394*, 187-194. Retrieved from <Go to ISI>://WOS:000425372500020. doi:10.1016/j.wear.2017.10.018

Jendel, T. (2002). Prediction of wheel profile wear-comparisons with field measurements. *Wear, 253*(1-2), 89-99. doi:10.1016/S0043-1648(02)00087-X

Kapoor, A., & Franklin, F. J. (2000). Tribological layers and the wear of ductile materials. *Wear, 245*(1-2), 204-215. doi:10.1016/S0043-1648(00)00480-4

Lewis, R., Braghin, F., Ward, A., Bruni, S., Dwyer-Joyce, R. S., Bel Knani, K., & Bologna, P. (2003). *Integrating dynamics and wear modelling to predict railway wheel profile evolution*. Paper presented at the 6th International Conference on Contact Mechanics and Wear of Rail/Wheel Systems, Gothenburg, Sweden.

Lewis, R., & Dwyer-Joyce, R. S. (2006). Wear at the wheel/rail interface when sanding is used to increase adhesion. *Proceedings of the Institution of Mechanical Engineers Part F Journal of Rail and Rapid Transit, 220*(1), 29-41. doi:10.1243/095440905x33260

Lewis, R., & Olofsson, U. (2004). Mapping rail wear regimes and transitions. *Wear, 257*(7-8), 721-729. doi:10.1016/j.wear.2004.03.019

Li, X., Jin, X. S., Wen, Z. F., Cui, D. B., & Zhang, W. H. (2011). A new integrated model to predict wheel profile evolution due to wear. *Wear, 271*(1-2), 227-237. doi:10.1016/j.wear.2010.10.043

Meghoe, A., Loendersloot, R., & Tinga, T. (2019). Rail wear and remaining life prediction using meta-models. *Interanational Journal of Rail Transportation, 8*(1), 1-26. doi:10.1080/23248378.2019.1621780

Santos, F. d. C., Santos Jr., A. A. d., & Bruni, F. (2004). Evaluation of Subsurface Contact Stresses in Railroad Wheels Using an Elastic Half-Space Model. *J. of the Braz. Soc. of Mech. Sci. & Eng., XXVI, No. 4 / 421*.

VI-Grade. (2016). *VI-Rail 17.0 Documentation*. Retrieved from Marburg, Germany: VI-grade GmbH

Zacher, M. (2009, 15 - 18 September). *Prediction of gauge corner cracking in rails for rail maintenance.* Paper presented at the Contact Mechanics, Florence, Italy.

Zobory, I. (1997). Prediction of wheel/rail profile wear. *Vehicle System Dynamics, 28*(2-3), 221-259. doi:10.1080/00423119708969355

APPENDIX

Table 2: Chemical composition of wheel and rail materials.

Material	C	Si	Mn	S	P	Ni	Cr	Mo	Cu	Sn	V
UIC 900A (R260)	0.73	0.26	1.06	0.026	0.009	0.01	0.01	0.01			
Class D tyre	0.65	0.24	0.71	0.046	0.026	0.15	0.18	0.03	0.26	0.031	
R7	0.52	0.40	0.80	0.035	0.035	0.05	0.30	0.08	0.30		0.05
R8T	0.54	0.36	0.80	0.006	0.003	0.14	0.13	0.045	0.14		
s1002	0.40	0.35	0.80	≤0.05	≤0.05						

Table 3: Input parameters for single scenario case.

Vertical wear depth of rail profile [mm]	**Curve radius [m]**	**Rail cant [mm]**	**Friction coefficient [-]**	**Vehicle speed [m/s]**	**Wagon mass [kg]**	**Longitudinal stiffness primary suspension [N/m]**	**Lateral stiffness primary suspension [N/m]**	**Material hardness [GPa]**
0	320	150	0.4	25	3.89E+04	6.17E+05	6.17E+05	2.7

Table 4: Input parameters for multiple scenarios.

	Vertical wear depth of rail profile [mm]	**Curve radius [m]**	**Rail cant [mm]**	**Friction coefficient [-]**	**Vehicle speed [m/s]**	**Wagon mass [kg]**	**Longitudinal stiffness primary suspension [N/m]**	**Lateral stiffness primary suspension [N/m]**	**Material hardness [GPa]**
1	0.53	1997.82	48.41	0.26	42.11	5.75E+04	2.13E+07	2.37E+07	3.34
2	7.84	3572.66	72.03	0.39	36.60	4.66E+04	5.04E+05	1.91E+07	2.74
3	9.96	1973.63	135.18	0.19	16.74	5.49E+04	2.66E+07	1.47E+07	3.35
4	6.05	1206.37	48.95	0.12	42.23	7.76E+04	1.31E+07	3.34E+07	3.23
5	2.98	1675.83	82.25	0.55	32.04	7.90E+04	7.28E+06	2.15E+06	3.29
6	7.40	1357.40	61.95	0.38	40.72	6.91E+04	1.26E+07	9.65E+06	2.83
7	2.02	3953.66	158.67	0.55	23.67	4.33E+04	3.06E+07	1.54E+07	3.14
8	12.12	1077.17	93.44	0.33	19.50	3.06E+04	2.77E+05	2.67E+07	3.26
9	0.71	1242.59	145.17	0.25	20.16	3.20E+04	3.49E+07	2.73E+07	2.97
10	5.38	1061.23	57.29	0.32	25.36	6.81E+04	1.09E+07	9.82E+06	3.30
11	10.24	1293.74	75.83	0.30	37.87	6.15E+04	1.26E+06	1.58E+07	2.94
12	3.62	3977.83	53.77	0.32	40.28	4.24E+04	1.08E+07	2.53E+07	2.89
13	8.36	1132.32	40.97	0.35	27.70	7.14E+04	3.79E+07	3.79E+07	2.76
14	4.45	1151.52	55.58	0.14	37.02	8.95E+04	2.74E+07	2.68E+07	3.40
15	12.27	3643.94	59.70	0.53	12.88	4.40E+04	3.73E+07	1.88E+07	2.76
16	11.59	1050.15	59.42	0.11	38.02	7.49E+04	9.55E+06	3.58E+07	3.11
17	5.12	1093.23	152.17	0.45	37.95	5.41E+04	3.86E+07	5.42E+06	2.94
18	1.07	1179.79	112.72	0.14	37.47	3.81E+04	2.85E+07	3.33E+07	3.17
19	9.91	1013.60	47.21	0.58	33.09	3.84E+04	6.95E+06	2.52E+07	3.28